NON-KEPLERIAN TRAJECTORY PLANNING VIA HEURISTIC-GUIDED OBJECTIVE REACHABILITY ANALYSIS

David A. Surovik and Daniel J. Scheeres

The University of Colorado at Boulder
Department of Aerospace Engineering Sciences
Boulder, CO, 80309, USA

ABSTRACT

In many space exploration scenarios of great interest, such as close-range orbits at asteroids and comets, spacecraft motion cannot be effectively approximated using Kepler's laws. Furthermore, special dynamical structures such as periodic orbits are not inherently associated with specific science requirements and serve only as a limited framework for facilitating operations. To broaden the mission design domain for pursuing abstract objectives in non-Keplerian systems, we instead formulate a reachability analysis tool that maps a subset of the extended phase space onto a set of high-level outcomes. As this process can only be conducted with numerical sampling, heuristics are used to guide iterative refinement of map features or the search for a performance metric's global maximum. The reachability data product can be visualized to aid preliminary mission design or efficiently computed onboard the spacecraft to enable opportunistic and robust online planning. Both modes of use are be demonstrated for planning scientifically motivated trajectories at the highly irregularly shaped comet 67/P.

Index Terms— autonomy, mission design, reachability, heuristic search, sampling-based planning

1. INTRODUCTION

Space exploration missions within dynamical regimes dominated by one nearly uniform gravity field, such as that of the Sun or a planet, rely heavily upon the conventional trajectory design techniques derived from Kepler's laws of orbital motion. However, ambitious missions to asteroids and comets face complex dynamics that cannot be adequately addressed with these techniques [1], motivating instead the consideration of automated algorithmic approaches more traditionally associated with the fields of robotics and AI planning [2].

Previously, exhaustive search techniques have been applied to mission design trade spaces such as launch and arrival dates – two inputs to Lambert's problem whose solution gives energy costs to be plotted on a "porkchop plot". Examples of numerical exploration of design spaces for non-Keplerian systems are generally applied to the paradigm case of the circular restricted three-body problem and focus on aspects such as phase space connectivity between special structures, e.g. periodic orbits and their stable/unstable manifolds [3], trajectory divergence rates [4], and more recently upon failure outcomes such as impact of the central body or escape from its vicinity [5]. By expending extensive numerical effort to study large swaths of the full domain of operations, this approach is naturally intended for preliminary mission design.

Conversely, analytic investigations have been conducted for the Kepler problem to characterize orbital reachability of targets from a given initial state with a single impulsive maneuver, key knowledge for quickly planning new operations in a mission that is already underway [6, 7]. These notions of reachability and numerical search have previously been combined in a computationally efficient manner to delineate safe and unsafe regions in the control domain of a spacecraft in a non-Keplerian system at a given initial state [8].

Recently, we have extended this work to include pursuit of science objectives in the analysis of reachable spacecraft motion [9], designed cost-to-go heuristics such that repeated application of the single-impulse maneuver design technique ultimately results in completion of extensive sets of prescribed tasks [10], and incorporated uncertainty mitigation through a balance of robust reachability analysis and reactive receding-horizon execution [11].

In this paper, we newly apply the heuristic mapping algorithm to temporally-extended control domains, which are especially appropriate for determining *when* to maneuver during online planning, as well as to other phase space subsets of interest for system analysis and preliminary mission design. Example maps are derived for a topical test case — motion planning for a close-proximity orbiter of comet 67/P Churyumov Gerasimenko (hereafter referred to simply as 67/P). Analysis will focus on fundamental issues such as safety conditions and trajectory divergence rates as well as upon science goals, consisting of geometric and temporal requirements for sets of close-range imaging tasks that target candidate lander deployment sites.

2. PROBLEM

2.1. Equations of Motion

In the test case system, close-proximity orbital motion is governed primarily by the central body's non-spherical gravity field. This force is most naturally expressed in the body-fixed frame, as are geometric constraints for imaging tasks. The spacecraft state $\mathbf{x}$, comprising position $\mathbf{r}$ and velocity $\dot{\mathbf{r}}$, evolves within this frame as:

$$\mathbf{x} = (\mathbf{r}, \dot{\mathbf{r}}) = \begin{bmatrix} x & y & z & \dot{x} & \dot{y} & \dot{z} \end{bmatrix}^T \tag{1}$$

$$\dot{\mathbf{x}} = (\dot{\mathbf{r}}, \ddot{\mathbf{r}}) = \mathbf{f}(\mathbf{x}) \tag{2}$$

$$\ddot{\mathbf{r}}(\mathbf{r}, \dot{\mathbf{r}}) = -\boldsymbol{\omega} \times (\boldsymbol{\omega} \times \mathbf{r}) - 2\boldsymbol{\omega} \times \dot{\mathbf{r}} + \mathbf{a}(\mathbf{r}; \mu, \mathcal{P}_\nu) \tag{3}$$

The body's angular velocity $\boldsymbol{\omega} = \omega\hat{\mathbf{z}}$ is constant and is oriented about the axis of greatest inertia, the minimum-energy rotation state; this produces centripetal and coriolis acceleration terms. The gravitational acceleration $\mathbf{a}$ of 67/P, and its Jacobian $\mathrm{d}\mathbf{a}/\mathrm{d}\mathbf{r}$, are computed from either a two-ellipsoid shape model or a polyhedral shape model $\mathcal{P}$ defined by a set of vertices and faces under an assumption of constant density and total gravitational parameter μ [12]. Unlike a spherical harmonic expansion, these models remains valid within the circumscribing sphere of the central body and do not involve truncation of high-order terms; instead the computational costs scale linearly with the number of ellipsoids or the polyhedron vertex count.

We note that, crucially, the numerical analysis employed in this paper can accommodate a "black box" dynamical model. This allows the potential to include other important forces as appropriate, such as third body tidal forces (e.g. in the Phobos system), solar radiation pressure (significant at very small bodies like asteroid Itokawa), and outgassing of volatiles as at 67/P during the span of its mission near perihelion. The first two of these examples can be seen in [9], and the latter may be a topic of future work — the present analysis assumes negligible outgassing as was the case during the initial rendezvous of the Rosetta spacecraft and the deployment of its lander Philae.

2.2. Anticipated Deviation

During the propagation of a trajectory, the state transition matrix $\Phi(t, t_0)$ can also be integrated to provide a linear description of the behavior of neighboring trajectories.

$$\Phi(t; t_0) = \int_{t_0}^{t} \frac{\mathrm{d}\mathbf{f}}{\mathrm{d}\mathbf{x}}\Big|_{\mathbf{x}(\tau)} \mathrm{d}\tau = \begin{bmatrix} \phi_{\mathbf{rr}}(t) & \phi_{\mathbf{rv}}(t) \\ \phi_{\mathbf{vr}}(t) & \phi_{\mathbf{vv}}(t) \end{bmatrix} \tag{4}$$

Using submatrices of Φ, the position deviation $\delta\mathbf{r}$ is expressed in terms of initial condition deviations:

$$\delta\mathbf{r}(t) = \phi_{\mathbf{rr}}(t; t_0)\delta\mathbf{r}(t_0) + \phi_{\mathbf{rv}}(t; t_0)\delta\mathbf{v}(t_0) \tag{5}$$

The robustness margin d is defined by parameterizing a worst-case realization of characteristic initial position and velocity deviation magnitudes σ_r and σ_v, obtained using the maximum eigenvalues of the position deviation propagation submatrices, with a scaling parameter η.

$$d(t) = \lambda_{max}(\phi_{\mathbf{rr}})\,\eta\sigma_r + \lambda_{max}(\phi_{\mathbf{rv}})\,\eta\sigma_v \tag{6}$$

As described at length in [11], this value can be used to provide guarantees, in the linear sense, that a prospective trajectory will still produce the desired outcome even under an anticipated amount of positional deviation, e.g. 3σ deviations by setting $\eta = 3$.

2.3. Mission Objectives

To avoid arbitrary reductions to the set of possible solutions, mission objectives are modeled not as target points $\mathbf{x}_i$ or reference trajectories $\tilde{\mathbf{x}}_i$ within state space, but as goal functions $g_i(\tilde{\mathbf{x}})$. This abstraction allows the design problem to encompass not only the question of how to reach a science orbit, but also what the science orbit should be in the first place — a particularly appropriate approach considering that motion is in general strongly non-periodic and uncertain. It also allows the implementation of many goal criteria without placing constraints on the precise sequencing or timing of goal completion.

The goal vector $\mathbf{g}$ tracks the status of a set of n_g objectives, whose values may be increased from 0 to 1 — indicating maximization or completion — by a potentially broad class of trajectories $\{\tilde{\mathbf{x}}\}_{g_i}$. Thus, the abstracted objective space is a unit cube of dimension n_g and when mapped into this space a successful mission profile $\mathbf{g}(\tilde{\mathbf{x}}_1, \tilde{\mathbf{x}}_2, \ldots, \tilde{\mathbf{x}}_n)$ traverses from the "bottom left" corner $\mathbf{g} = \mathbf{0}$ to the "top right" corner $\mathbf{g} = \mathbf{1}$.

2.3.1. Observation Goals

As in the bulk of our investigations to-date, the objectives g_i are defined for close-range imaging of a set of points of interest $\mathbf{R}_i$ located on the body surface. Each i'th task (multiple tasks may share a target) is defined as the simultaneous fulfillment of upper (a^+) and lower (a^-) bounds of several objective metrics $a(\mathbf{x})$ for a duration Δt_g. These metrics comprise the spacecraft's target-relative range ρ_i, co-elevation θ_i, azimuth φ_i, and solar phase angle ψ_i computed from its relative position $\boldsymbol{\rho}_i = \mathbf{r} - \mathbf{R}_i$ and the east-north-up basis vectors $(\hat{\mathbf{e}}, \hat{\mathbf{n}}, \hat{\mathbf{u}})_i$ of the target's local frame.

$$\rho_i = |\boldsymbol{\rho}_i(t)|_2 \tag{7}$$

$$\theta_i = \cos^{-1}(\hat{\boldsymbol{\rho}}_i(t) \cdot \hat{\mathbf{u}}_i) \tag{8}$$

$$\varphi_i = \tan^{-1}\left[\frac{\hat{\boldsymbol{\rho}}_i(t) \cdot \hat{\mathbf{e}}_i}{\hat{\boldsymbol{\rho}}_i(t) \cdot \hat{\mathbf{n}}_i}\right] \tag{9}$$

$$\psi_i = \cos^{-1}(\hat{\boldsymbol{\rho}}_i(t) \cdot \hat{\boldsymbol{\rho}}_s(t)) \tag{10}$$

As the Sun-pointing vector $\hat{\boldsymbol{\rho}}_s$ is approximated as constant in the inertial frame but periodic in the body-fixed rotating frame, ψ_i applies temporal constraints.

For robust planning, the bounds a^+ and a^- for each parameter are reduced by an amount such that $\breve{a}^-(d(t)) < a(\mathbf{x}) < \breve{a}^-(d(t)) \Rightarrow a^- < a(\mathbf{x} + d(t)\hat{\mathbf{n}}) < a^+$ for any unit vector $\hat{\mathbf{n}}$. In other words, if the nominal path satisfies the reduced bounds $(\breve{a}^-, \breve{a}^+)$, any path that deviates less than the margin $d(t)$ will still satisfy the nominal constraint bounds.

2.3.2. *Operational Constraints*

With $\rho_{\mathcal{P}} = \min \rho(\mathbf{x}, \mathcal{P})$ denoting the shortest range to any face of the polyhedron $\mathcal{P}$ or any point on the surface of an ellipsoid, we define bounds $\rho_{\mathcal{P}}^- < \rho_{\mathcal{P}} < \rho_{\mathcal{P}}^+$ within which operations are permitted for scenarios other than landing. The lower bound acts as a margin of error against impact, while the upper bound prevents undesirable excursions away from the orbit regime of interest. Other concerns such as fuel consumption Δv and trajectory duration Δt can be included as soft constraints in a decision metric, i.e. a function that scalarizes the multiple objectives, constraints, and the cost-to-go into a single function.

2.4. Test Scenario

Comet 67/P is chosen as an illustrative system on account of its exceptionally irregular shape. Although the black-box dynamical model could readily accommodate outgassing forces, third-body gravitation, and solar radiation pressure, these are presently omitted for simplicity. The comet has a mass of 10^{13} kg and mean radius $\bar{R} = 1.7$ km, corresponding to a mean density of 0.47 g/cm^3, while its largest dimension spans 4.3 km. Rotation occurs about its axis of greatest inertia, which has obliquity 52°, with a period of $2\pi/\omega = 12.4$ hr. This is roughly equivalent to the period of a Keplerian orbit with semimajor axis equal to $2\bar{R}$.

Observation targets correspond to three of the candidate landing sites considered by for ESA's Philae lander, namely the actual target Site J on the smaller lobe of the comet, the backup Site C on the perimeter of the larger lobe, and an earlier candidate Site A on the inner surface of the larger lobe. All observation tasks have range bounds $\rho^- = 0.85$ km, $\rho^+ = 1.15$ km and phase angle bounds $\psi^- = 30°$, $\psi^+ = 60°$, affording close views with moderate shadows to best reveal surface features. The imaging duration is set at $\Delta t_g = 2$ minutes. Four tasks are assigned per site: one from within $\theta^+ = 20°$ of the surface normal, and three from between $\theta^- = 30°$ and $\theta^+ = 60°$ with additional azimuthal constraints producing evenly spaced 60° segments. System geometry is shown in Fig. 1.

3. PHASE SPACE MAPPING

3.1. Domain

Due to factors that are asynchronous with the rotation period of the body frame — solar phasing in this case, and third body gravitation and solar radiation pressure in other systems of interest — the predictive model is a nonautonomous system and the extended phase space must be considered. Combining 3D position $\mathbf{r}$, velocity $\mathbf{v}$, and scalar initial time t, this space is seven-dimensional, which is not amenable to numerical search or visualization/user comprehension. Thus, both preliminary mission analysis and online planning must deal with lower-dimensional subsets of the extended phase space, $\mathcal{M} \subset (\mathcal{X} \times \mathcal{T})$, ideally in two or three dimensions.

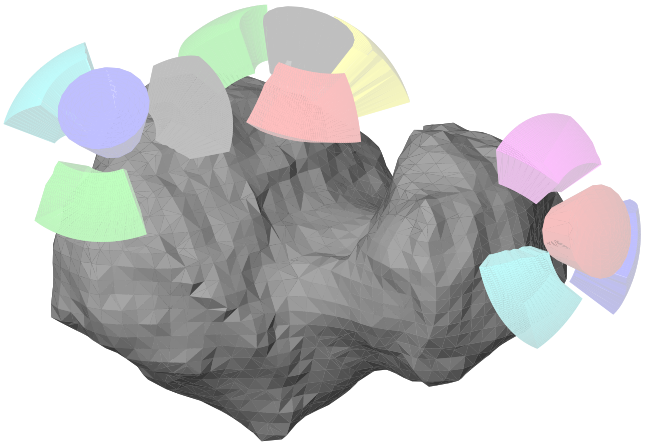

Fig. 1. Polyhedral shape model of 67/P and observation objective regions.

These reduced spaces could be defined by a straightforward combination of a subset of position and velocity axes with a timing element, e.g. (t, y, v_x), with the remaining state variables substituted from a reference state $(t_0, \mathbf{x}_0)$. Alternately, manifolds could be described via some transformation $T : (t_0, \mathbf{x}_0, \mathbf{u}_i) \to (t, \mathbf{x})$ with $\mathbf{u}_i$ a coordinate along the manifold from within a set $\mathcal{U}$ and $(t, \mathbf{x}) \in \mathcal{M}$. This could be used to parameterize the search domain in terms of derived values such as Jacobi energy, osculating orbital element values, or alternate Cartesian descriptions such as the radial/in-track/cross-track frame. Some such reduced design spaces will be investigated in the following sections; first, we will detail the process for efficient numerical search and mapping of the domain $\mathcal{U}$.

3.2. Heuristic Search and Mapping

As has been comprehensively detailed in [10], the search method consists of an iterative refinement process repeatedly applied after initializing the search with either a random or evenly-spaced low-resolution sampling of the search domain $\mathcal{U}$, whose axes correspond to the parameters that define $\mathcal{M}$:

1. Numerically propagate trajectories resulting from the newest samples of the search manifold $\{\mathbf{u}_i\} \in \mathcal{U}$
2. Evaluate mission-relevant outcomes of each trajectory, e.g. constraint satisfaction and objective completion

3. Use all existing samples $\mathbf{u}_i$ to recompute a triangulation of the space $\mathcal{U}$ as a set of simplices (triangular or tetrahedral elements) bounded by sample points

4. Designate next sample set probabilistically via the search heuristic

The heuristic itself consists of a weighting function W computed for each simplex,

$$\nu_j = \{i_{j,1}, i_{j,2}, i_{j,3}, i_{j,4}\} \tag{11}$$

as the product of three characteristic factors:

$$W_j = \text{volume}\,(\nu_j) \cdot \left(\underset{i \in \nu_j}{\text{mean}}\,\{t_i\}\right) \cdot S\,(\nu_j)^{P(\tau)} \tag{12}$$

Each term serves a specific role in transforming the probability distribution function that governs selection of the next sample set. Given in order, these terms represent:

- **Simplex volume** — normalizing weight by volume flattens the probability distribution across the continuous control domain
- **Mean trajectory lifespan** — bias is then applied to regions that produce longer-lived trajectories, implying potentially heightened complexity
- **Search/partitioning** — additional bias is finally applied to maximize a user-defined function $S\,(\nu)$ designed to draw out the desired details of the map

The final factor is also modulated by an exponent P that increases as a function of the search progress factor τ, which itself increases from 0 to 1 as the specified search resolution is approached.. This progressively strengthens the bias of the search toward high-performing regions in a manner akin to simulated annealing.

For preliminary mission design and analysis, visualizations are needed that illustrate the correspondence of $\mathbf{u}$ with various outcome values $\mathbf{y}\,(\tilde{\mathbf{x}})$ such as safety status and goal progression. In this case, the function $S\,(\nu)$ can be designed to increase in proportion to the variation of specified elements of $\mathbf{y}$ across a given simplex ν_j. Fig. 2 shows the increased clarity of features on the $\mathcal{U} \rightarrow \mathcal{Y}$ reachability map that can be attained at a fixed sample count by applying such a heuristic.

Conversely, an autonomously operating spacecraft is less concerned with global partitioning and instead must merely strive to maximize some decision function $s\,(\mathbf{u})$. By defining s in accordance with mission requirements and performance considerations, using a function q whose field augments the $\mathcal{U} \rightarrow s$ map with smooth slopes (for "hill-climbing" search) and defining the simplex value function as

$$S\,(\nu) = \max_{i \in \nu}\,[s\,(\mathbf{u}_i) + q\,(\mathbf{u}_i)] \tag{13}$$

much larger values of s can rapidly be located by heuristic search than is possible with a naive search, as illustrated in Fig. 3.

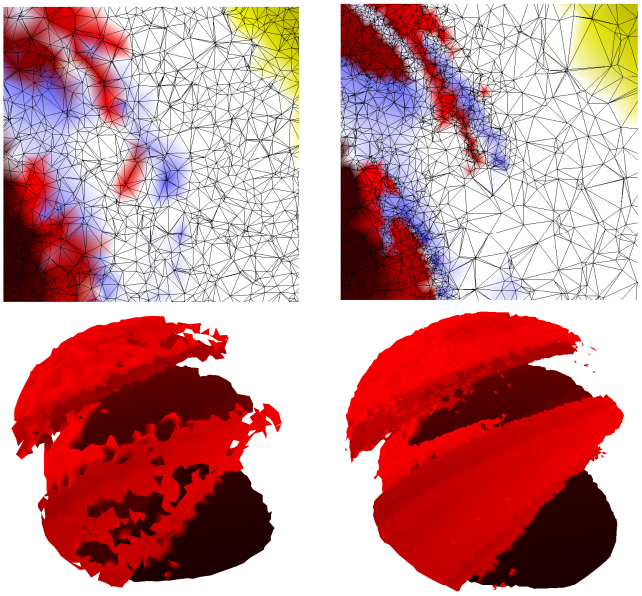

(a) Naive search (b) Heuristic search

Fig. 2. Numerical mapping between a phase space domain and abstract outcome space charting impact and escape scenarios (red and yellow) as well as goal progression (blue) — comparison of computationally inefficient approach based on uniform sample distribution and efficient approach based on adaptive sample distribution. Reproduced from [9].

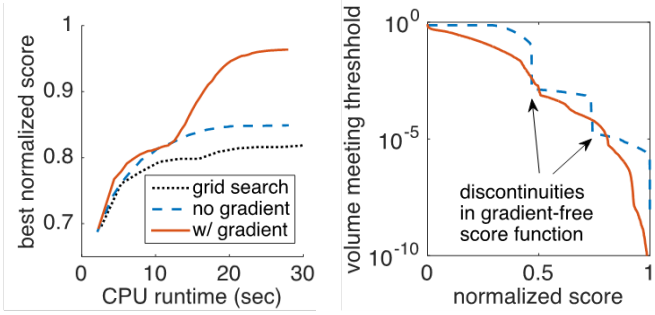

(a) Performance (b) Search sparsity

Fig. 3. Performance of numerical search of a map between a phase space domain and decision metric space — comparison of computationally inefficient approach based on uniform sample distribution and efficient approach based on adaptive sample distribution with gradient-climbing component. Plot (b) shows the vanishingly small portion of $\mathcal{U}$ that produces large values of s. Reproduced from [10].

4. PRELIMINARY MISSION ANALYSIS

As mentioned above, the heuristic mapping of initial condition sets to high-level outcomes can be used during preliminary mission design and analysis to illustrate the unintuitive phenomena that occur in strongly non-Keplerian systems. The scenario examined here is the use of medium-proximity orbits as a jumping off point from which to plan very close proximity trajectories through objective regions.

Objective reachability is mapped from three such orbits propagated from initial conditions with zero osculating eccentricity and a radius 1.75 times that of the extremum of the central body — one polar orbit, one retrograde orbit (both of which are nearly periodic), and one prograde orbit (which is not nearly periodic) all shown in Fig. 4. The 3D control domain consists of timing (the selection of an initial point along the nominal orbit), in-track Δv, and cross-track Δv.

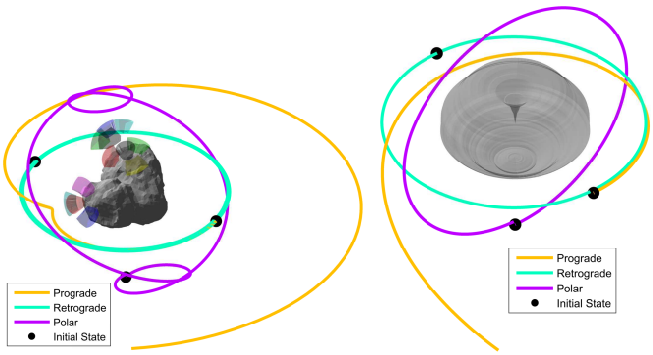

(a) Rotating frame (b) Inertial frame

Fig. 4. Nominal prograde, retrograde, and polar orbital trajectories used for defining three reachable domains with timing elements.

The reachability maps $\mathcal{U} \rightarrow \mathcal{Y}$ for these three scenarios are given in Fig. 5 in two forms: selected simplices of the full 3D domain are shown alongside reduced 2D domains that reflect narrower time ranges and zero cross-track Δv. In all cases, resonant effects are clearly observed by alternatingly colored swaths of $\mathbf{u}$ values that correspond to impact of the two different lobes of 67/P. Furthermore, as the 2D sections reveal and as intuition implies, impact scenarios are only observed when the in-track velocity is decreased, while a sufficient increase uniformly results in escape. Goal fulfillment is not observed for operations in the equatorial plane as most goal regions are defined in the northern hemisphere.

In the reachability map of the polar orbit domain, the abundance of goal regions near the extrema of the timing axis indicates that goal reachability is maximal when maneuvers are executed above the south pole of the central body. This reflects the large degree of control over phasing that can be achieved by rotating the orbit plane about the polar axis, combined with the fact that all goals are defined north of the

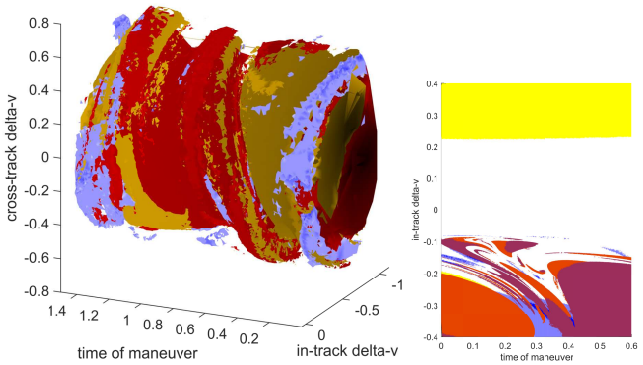

(a) Polar orbit

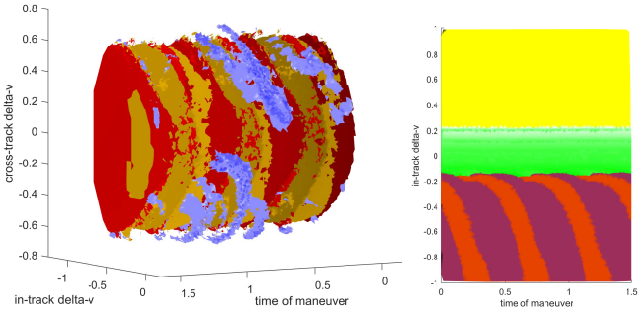

(b) Retrograde orbit

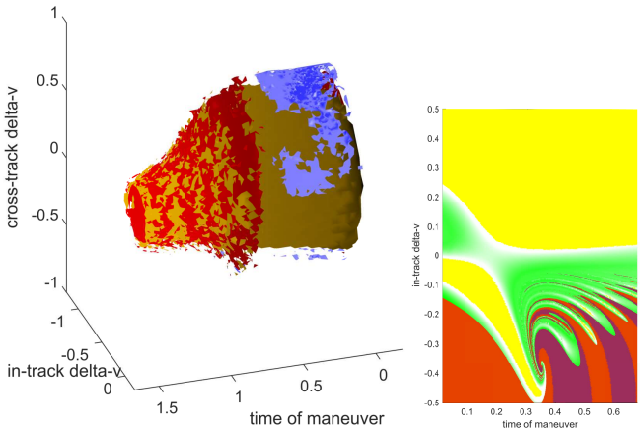

(c) Prograde orbit

Fig. 5. Reachable sets under timing, in-track, and cross-track impulsive control authority from three different nominal trajectories. Left images show 3D structure of sets that cause impact of either central body lobe (red, orange) or satisfaction of mission goals (blue). Right images show high-detail results in small 2D regions, with additional light blue and white regions indicating safe boundedness while yellow regions indicate escape. In lieu of substantive goal fulfillment regions, green regions indicate relative stability.

body's equator. Similarly, the corkscrew shape of the impacting sets further reflects the misalignment of the spacecraft orbit plane with the central body's rotation plane.

Conversely, the impact set for the retrograde orbit shows fast periodicity along the time axis, indicating that several orbits are completed in the body-fixed frame even though only one is complete in the inertial frame — this also demonstrates stability as perturbing effects are rapidly averaged out. The modulation of the goal set along this axis with period one reflects the influence of the solar phasing requirement in the science specifications. Lastly, the prograde orbit reachability map shows less regularity of structure due to the strong non-periodicity of the nominal orbit.

5. AUTONOMOUS ONLINE PLANNING

The heuristic reachability analysis tool is appropriate for planning a single impulsive maneuver based upon a given initial state or nominal trajectory. However, an extensive set of mission objectives would require many such maneuvers, and consideration of the likelihood that a prospective trajectory will ensure further opportunities for progress in the next planning cycle. Given the complexity of planning even a single maneuver, this decision-making process is made tractable by planning one maneuver at a time in an autonomous, receding-horizon approach characteristic of Model Predictive Control — preferably implemented onboard the spacecraft itself in order to avoid communication resource usage and delays.

As described in [10, 11], a key component in enabling this mode of operation is the formulation of an effective *prospect heuristic* h_p, similar to a cost-to-go function. A simple implementation of h_p has been designed based upon analyses such as that of Fig. 5(a) as well as Keplerian intuitions. The implementation from [11] includes two components, such that $h_p\left(\mathbf{x}(t)\right)$ peaks when the spacecraft orbit radius crosses the value used for the reference orbits of the previous section, and also when the latitude approaches $-90°$ — a combination of factors that the reachability map indicated to broaden prospects. This value is then included in the formulation of the decision metric s to balance goal progression against longer-term concerns such as these and to determine the time at which to begin the next planning cycle.

$$s\left(\mathbf{u}\right) = \max_{t \,\in\, T_{safe}} \left[\Delta g\left(\tilde{\mathbf{x}}\left(t\right)\right) + h_p\left(\mathbf{x}\left(t\right)\right)\right] \qquad (14)$$

Notably this value also enforces additional constraints via the timespan T_{safe} such that subsequent maneuvers may not happen too rapidly nor too late, allowing time for convergence of state estimation and the computation of a subsequent plan but without lingering long enough to approach a failure scenario or the end of the predicted trajectory. When T_{safe} is empty, safety violations would occur more quickly than a new plan could be formulated; in these cases $s = 0$ is enforced.

Combined with the robustness criteria from section 2.2, complete mission profiles are produced as seen in Fig. 6.

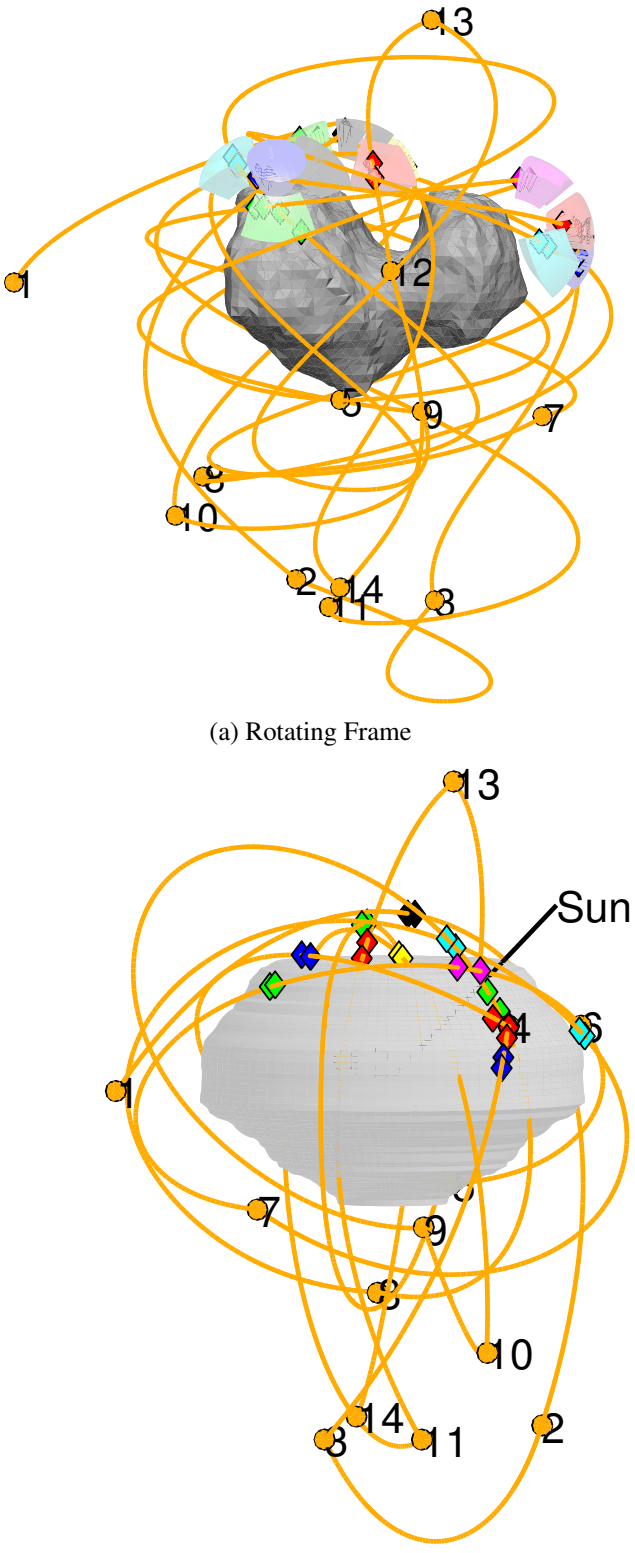

(a) Rotating Frame

(b) Inertial Frame

Fig. 6. Example mission profile generated by receding-horizon application of autonomous robust reachability-based maneuver planning. Reproduced from [11].

6. CONCLUSION

Enabled by appropriate calibration of a search heuristic and a black-box predictive model that includes high-level mission outcomes, numerical reachability analysis appears to be a compelling tool for mission design in unintuitive, strongly non-Keplerian systems. This method could be applied during preliminary design and analysis in order to elucidate the effects of challenging phenomena such as highly inhomogeneous gravity fields, orbit resonances, and solar phasing of observations.

Alternatively, the method could also be applied online to produce sequences of maneuvers that ultimately fulfill large sets of mission goals all while mitigating uncertainty via robustnes considerations and reacting to unacceptably off-nominal conditions. Both modes of analysis are appropriate for an objective-based mission design philosophy that centers upon exploitation of the strongly perturbed natural dynamics of the system rather than continuously expending guidance efforts upon merely overpowering them.

7. REFERENCES

[1] Marco B. Quadrelli, Lincoln J. Wood, Joseph E. Riedel, Michael C. McHenry, MiMi Aung, Laureano A. Cangahuala, Richard A. Volpe, Patricia M. Beauchamp, and James A. Cutts, "Guidance, navigation, and control technology assessment for future planetary science missions," *Journal of Guidance, Control, and Dynamics*, vol. 38, no. 7, pp. 1165–1186, May 2015.

[2] Joseph A. Starek, Behet Aikmese, Issa A. Nesnas, and Marco Pavone, *Spacecraft Autonomy Challenges for Next-Generation Space Missions*, vol. 460 of *Lecture Notes in Control and Information Sciences*, pp. 1–48, Springer Berlin Heidelberg, 2016.

[3] Jeffrey S. Parker and Rodney L. Anderson, *Low-Energy Lunar Trajectory Design*, chapter 2, Wiley, 2014.

[4] B.F. Villac, "Using fli maps for preliminary spacecraft trajectory design in multi-body environments," *Celestial Mechanics and Dynamical Astronomy*, vol. 102, no. 1-3, pp. 29–48, 2008.

[5] A. Utku, L. Hagen, and P. Palmer, "Initial condition maps of subsets of the circular restricted three-body problem phase space," *Celestial Mechanics and Dynamical Astronomy*, vol. 123, no. 4, pp. 387–410, 2015.

[6] Gang Zhang, Xibin Cao, and Guangfu Ma, "Reachable domain of spacecraft with a single tangent impulse considering trajectory safety," *Acta Astronautica*, vol. 91, pp. 228–236, 2013.

[7] Changxuan Wen, Yushan Zhao, Peng Shi, and Zhang Hao, "Orbital accessibility problem for spacecraft with a single impulse," *Journal of Guidance, Control, and Dynamics*, vol. 37, no. 4, pp. 1260–1271, 2014.

[8] E. Komendera, J. Garland, E. Bradley, and D.J. Scheeres, "Efficiently evaluating reachable sets in the circular restricted 3-body problem," *IEEE Transactions on Aerospace and Electronic Systems*, vol. 51, no. 1, pp. 454–467, January 2015.

[9] David A Surovik and Daniel J Scheeres, "Adaptive reachability analysis to achieve mission objectives in strongly non-keplerian systems," *Journal of Guidance, Control, and Dynamics*, vol. 38, no. 3, pp. 468–477, 2015.

[10] David A. Surovik and Daniel J. Scheeres, "Heuristic search and receding-horizon planning in complex spacecraft orbit domains," in *Proceedings of the International Conference on Automated Planning and Scheduling*. 2015/06/07 2015, Association for the Advancement of Artificial Intelligence Press.

[11] David A Surovik and Daniel J Scheeres, "Reactive and robust paradigms for autonomous mission design at small bodies," in *Proceedings of the AAS/AIAA Astrodynamics Specialist Conference*, 2016, number American Astronautical Society Paper Number 16-412, Napa, CA.

[12] Daniel. J. Scheeres, *Orbital Motion in Strongly Perturbed Environments*, chapter 2, Praxis Springer, 2012.